

1 **Chromosomal assembly and analyses of genome-wide recombination rates**
2 **in the forest pathogenic fungus *Armillaria ostoyae***

3

4 Renate Heinzlmann^{a,b*}, Daniel Rigling^a, György Sipos^c, Martin Münsterkötter^{c,d}, Daniel Croll^e

5

6 ^aSwiss Federal Research Institute WSL, Zürcherstrasse 111, CH-8903 Birmensdorf, Switzerland

7 ^bDepartment of Forest and Conservation Sciences, The University of British Columbia, 2424 Main
8 Mall, Vancouver, BC, V6T 1Z4, Canada

9 ^cFunctional Genomics and Bioinformatics Group, Research Center for Forestry and Wood Industry,
10 University of Sopron, Bajcsy-Zsilinszky. u. 4, H-9400, Sopron, Hungary

11 ^dInstitute of Bioinformatics and Systems Biology, Helmholtz Zentrum München (GmbH), Ingolstädter
12 Landstrasse 1, D-85764 Neuherberg, Germany

13 ^eLaboratory of Evolutionary Genetics, Institute of Biology, University of Neuchâtel, Rue Emile-
14 Argand 11, CH-2000 Neuchâtel, Switzerland

15

16 * Corresponding author: renate.heinzlmann@ubc.ca

17

18

19

20

21

22 Author contributions: RH and DC conceived the study; RH analyzed the data; DR, GS and MM
23 provided datasets; RH and DC wrote the manuscript.

24

25

26

27

28 **Abstract**

29 Recombination shapes the evolutionary trajectory of populations and plays an important role in
30 the faithful transmission of chromosomes during meiosis. Levels of sexual reproduction and
31 recombination are important properties of host-pathogen interactions because the speed of antagonistic
32 co-evolution depends on the ability of hosts and pathogens to generate genetic variation. However, our
33 understanding of the importance of recombination is limited because large taxonomic groups remain
34 poorly investigated. Here, we analyze recombination rate variation in the basidiomycete fungus
35 *Armillaria ostoyae*, which is an aggressive pathogen on a broad range of conifers and other trees. We
36 constructed a dense genetic map using 198 single basidiospore progeny from a cross. Progeny were
37 genotyped at a genome-wide set of single nucleotide polymorphism (SNP) markers using double
38 digest restriction site associated DNA sequencing (ddRADseq). Based on a linkage map of on 11,700
39 SNPs spanning 1007.5 cM, we assembled genomic scaffolds into 11 putative chromosomes of a total
40 genome size of 56.6 Mb. We identified 1984 crossover events among all progeny and found that
41 recombination rates were highly variable along chromosomes. Recombination hotspots tended to be in
42 regions close to the telomeres and were more gene-poor than the genomic background. Genes in
43 proximity to recombination hotspots were encoding on average shorter proteins and were enriched for
44 pectin degrading enzymes. Our analyses enable more powerful population and genome-scale studies of
45 a major tree pathogen.

46

47 Key words: double digest restriction site-associated DNA sequencing (ddRADseq), high-resolution
48 genetic map, recombination hotspots, host-pathogen interaction, *Armillaria ostoyae*

49

50

51 **Introduction**

52

53 Recombination shapes the evolution of chromosomes and the evolutionary trajectory of
54 populations (Haenel *et al*, 2018; Otto and Lenormand, 2002). Crossovers enable the pairing and proper
55 disjunction of homologous chromosomes during meiosis and are essential for the long-term
56 maintenance of chromosomal integrity (Fledel-Alon *et al*, 2009; Hassold and Hunt, 2001). Loss of
57 recombination on chromosomes is often associated with degenerative sequence evolution including
58 gene loss and deleterious rearrangements. For example, the consequences of recombination cessation
59 largely shaped the evolution of sex chromosomes and mating-type regions in animal, plants and fungi
60 (Charlesworth *et al*, 2000; Wilson and Makova, 2009). Recombination also has a fundamental impact
61 on the organization of genetic variation within populations. Recombination breaks up linkage between
62 alleles at different loci, thereby generating novel combinations across loci that can be exposed to
63 selection. Decreased linkage between loci increases the efficacy of selection and, hence, promotes
64 adaptation (Hill and Robertson, 2009; Otto and Barton, 1997; Otto and Lenormand, 2002). However,
65 recombination can also break up linkage between co-adapted alleles across loci, thereby creating a
66 potential evolutionary conflict.

67

68 The study of the role of sex and levels of recombination is particularly important for our
69 understanding of coevolutionary arms races in host-pathogen interactions. Host populations are
70 thought to be under strong selection to maintain sexual reproduction to escape co-evolving pathogens
71 by generating novel genotypes (Hamilton, 1980; Lively, 2010; Morran *et al*, 2011). Similarly,
72 pathogens are under strong selection pressure to adapt to resistant hosts. In addition to mutation rates,
73 the level of recombination is likely under selection in pathogen populations (Croll *et al*, 2015; Möller
74 and Stukenbrock, 2017; Sánchez-Vallet *et al*, 2018). Notable cases of pathogen emergence driven by
75 recombination include epidemic influenza viruses (Nelson and Holmes, 2007), typhoid fever caused
76 by *Salmonella enterica* (Didelot *et al*, 2007; Holt *et al*, 2008) and toxoplasmosis caused by
77 outcrossing *Toxoplasma gondii* strains (Wendte *et al*, 2010). Sexual reproduction is also prevalent in
78 many fungal plant pathogens playing an important role in adaptive evolution (Möller and Stukenbrock,

79 2017). In particular in crop pathogens, the level of recombination was proposed as a predictor for the
80 speed at which the pathogen will overcome host resistance (McDonald and Linde, 2002; Stukenbrock
81 and McDonald, 2008). While pathogens of crop received significant attention to elucidate the
82 organization of genetic variation and the impact of recombination on genome evolution (Croll *et al*,
83 2015; Stukenbrock and Dutheil, 2018), the role of recombination in the evolution of tree pathogens or
84 saprophytes is still largely unknown.

85

86 An important group of fungal tree pathogens and saprophytes is represented by the basidiomycete
87 genus *Armillaria*. The numerous fungi of this genus play an important role in the dynamics of forest
88 ecosystems worldwide (Heinzelmann *et al*, 2019; Shaw III and Kile, 1991). With their ability to
89 degrade all structural components of dead wood causing a white-rot, *Armillaria* species contribute
90 significantly to nutrient cycling in forest ecosystems (Hood *et al*, 1991). Moreover, *Armillaria* species
91 act as facultative pathogens infecting the root systems of healthy or weakened trees, and eventually
92 cause tree mortality (Guillaumin *et al*, 2005). In timber plantations, the presence of *Armillaria* root
93 disease causes substantial economic losses (Laflamme and Guillaumin, 2005), whereas in natural
94 forest ecosystems the disease impacts forest succession, structure and composition (Bendel *et al*, 2006;
95 Hood *et al*, 1991; McLaughlin, 2001). In the Northern Hemisphere, *Armillaria ostoyae* is of special
96 importance. It is widely distributed in North America and Eurasia and recognized as an aggressive
97 pathogen on a broad range of conifers and other trees (Anderson and Ullrich, 1979; Guillaumin *et al*,
98 1993; Morrison *et al*, 1985; Ota *et al*, 1998; Qin *et al*, 2007). *A. ostoyae* challenges current
99 containment strategies and the search for new control strategies is ongoing (Heinzelmann *et al*, 2019).

100

101 *Armillaria* spp. have relatively large and recently expanded genomes (Aylward *et al*, 2017; Sipos
102 *et al*, 2017). Recently, the genomes of a European and a North American *A. ostoyae* strain were
103 published (Sipos *et al*, 2017). The genome assembly of the European strain (SBI C18/9) is of 60.1 Mb
104 and split into 106 scaffolds. The genome assembly for the North American strain (28-4) is similar in
105 length (58.0 Mb) but considerably more fragmented. However, none of the to date published
106 *Armillaria* genomes is yet assembled to chromosome-scale sequences (Collins *et al*, 2013; Sipos *et al*,

107 2017; Wingfield *et al*, 2016). Expanded gene families in *Armillaria* include pathogenicity-related
108 genes, enzymes involved in lignocellulose-degradation and *Armillaria*-specific genes with mostly
109 unknown functions (Sipos *et al*, 2017). Interestingly, in comparison with other white-rot fungi,
110 *Armillaria* shows an under-representation of ligninolytic gene families and an overrepresentation of
111 pectinolytic gene families (Sipos *et al*, 2017). *A. ostoyae* is out-crossing and progeny populations were
112 successfully used to identify the genetic basis of a major colony morphology mutant phenotype
113 (Heinzelmann *et al*, 2017). However, further insights into genome evolution of *Armillaria* and the
114 genetic basis of phenotypic traits are hampered by a lack of a dense recombination map and a fully
115 finished reference genome.

116

117 In this study, we first aimed to establish a chromosome-scale assembly for *A. ostoyae* using a
118 dense recombination map. Second, we aimed to test for variation in recombination rates within and
119 among chromosomes to identify putative recombination hotspots. Finally, we analyzed genomic
120 correlates of recombination rate variation including GC-content, gene density and content of
121 transposable elements.

122

123

124 **Material and Methods**

125

126 *Mapping population, construction of genetic map and comparison with reference genome*

127 The mapping population used in this study consisted of 198 single basidiospore progeny of the
128 diploid *A. ostoyae* strain C15 (WSL Phytopathology culture collection number: M4408). This strain
129 was collected from a Scots pine (*Pinus sylvestris*) situated in a forest stand in the Swiss Plateau
130 (Prospero *et al*, 2004). The haploid progeny were obtained from a single basidiocarp obtained *in vitro*
131 as described previously (Heinzelmann *et al*, 2017). The haploid progeny and the diploid parent were
132 genotyped at a genome-wide set of single nucleotide polymorphism (SNP) markers making use of
133 double digest restriction site associated DNA sequencing (ddRADseq). The genetic map was
134 constructed *de novo* using R/ASMap version 0.4-4 (Taylor and Butler, 2017) which is based on the

135 MSTmap algorithm of Wu *et al* (2008). The significance threshold was set to $P = 10^{-5}$. The marker
136 order in the final genetic map was compared to the order in the genome of the haploid *A. ostoyae*
137 strain SBI C18/9 (assembly version 2, May 2016, Sipos *et al*, 2017). Strain SBI C18/9 (WSL
138 Phytopathology culture collection number: M9390) originates from Switzerland but is unrelated to
139 strain C15.

140

141 *Construction of chromosome-scale sequences*

142 The scaffolds of the reference genome were assembled into near chromosome-scale sequences,
143 hereafter termed pseudochromosomes, based on the order of scaffolds within linkage groups.
144 Scaffolds which were split by the genetic map into fragments mapping to different linkage groups or
145 well separated regions (i.e. > 650 kb apart) of a linkage group were broken up into fragments.
146 Emerging, unanchored sequences were removed. Scaffolds (or fragments thereof) that were joined into
147 pseudochromosomes were separated by gaps of 10 kb. Scaffolds and scaffold fragments which were
148 not oriented by the genetic map were orientated randomly. The completeness of both the original
149 genome assembly and the pseudochromosomes and the corresponding gene annotations was compared
150 with BUSCO version 3.1.0 (Simão *et al*, 2015) using the Basidiomycota dataset (library
151 basidiomycota_odb9).

152

153 *Count and distribution of crossover events*

154 The number of crossover events per progeny and pseudochromosome was extracted from the
155 genetic map using the countXO function of the R/qtl package, version 1.40-8 (Broman *et al*, 2003).
156 We used locateXO (R/qtl) to identify the position of crossover events and extract flanking markers.
157 For each crossover event, we calculated the physical distance of the two flanking markers. To check
158 for the presence of potential non-crossover (= non-reciprocal recombination events), the distance of
159 two consecutive crossover events on a pseudochromosome was calculated. We assessed the minimal
160 distance of crossover events as the physical distance between the first marker following a crossover
161 and the last marker before the next crossover.

162

163 *Recombination rate variation along pseudochromosomes*

164 For each pseudochromosome, the recombination rate was estimated in non-overlapping 20 kb
165 segments as follows. First, genetic positions were linearly interpolated every 20 kb based on genetic
166 and physical positions of markers using the `approx` function of the R package 'stats', version
167 3.4.0 (R Development Core Team, 2017). Next, the genetic distance per segment was calculated as the
168 difference in genetic distance of the end and start point of the segment. Finally, the recombination rate
169 per segment was obtained by dividing the interpolated genetic distance by the segment size. A
170 segment size of 20 kb was considered appropriate because the physical distance between consecutive
171 markers (excluding marker pairs with a distance of ≤ 400 bp to avoid spurious marker resolution
172 through markers associated with the same restriction site) was less than 10 kb for ~50% of marker
173 pairs, and less than 20 kb for ~75% of the marker pairs (Figure 1). We tested for heterogeneity of
174 recombination rate along the pseudochromosomes by comparing the observed distribution of
175 recombination rates per segment with the expected distribution using Fisher's exact test. For this, the
176 20 kb segments were binned into categories of 0, 1, 2, 3, 4, 5, 6-15 cM. A Poisson distribution with
177 lambda equaling the average cM per segment was used as the expected distribution. *P*-values were
178 estimated by Monte Carlo simulations with 10^6 replicates. This test was conducted for each
179 pseudochromosome independently and all pseudochromosomes together.

180

181 *Identification and characterization of recombination hotspots*

182 We identified recombination hotspots in the genome by searching for 20 kb segments with
183 unusually high recombination rates (i.e. ≥ 200 cM/Mb). To account for the uncertainty in the
184 identification of exact crossover locations, 20 kb segments with recombination rates ≥ 200 cM/Mb
185 were conservatively extended by 15 kb on each side to define 50 kb recombination hotspot windows.
186 In cases where two adjacent 20 kb segments had recombination rates ≥ 200 cM/Mb, one 50 kb hotspot
187 centered on the two segments was created. Hotspots overlapping with assembly gaps were excluded.
188 We assessed the correlation of GC-content, as well as gene and transposable element density with
189 recombination hotspots. For this, the pseudochromosomes were divided into non-overlapping 50 kb
190 segments. Segments were analyzed for GC-content and percentage of gene and transposable element

191 coverage. Transposable elements were identified and annotated with RepeatModeler version 1.0.8 (A.
192 F. A. Smit and R. Hubley, RepeatModeler Open-1.0 2008–2015; <http://www.repeatmasker.org>) and
193 RepeatMasker version 4.0.5 (A. F. A. Smit, R. Hubley, and P. Green, RepeatMasker Open-4.0 2013–
194 2015; <http://www.repeatmasker.org>).

195

196 In addition, we assessed the correlation of recombination hotspots with certain gene properties
197 and functions. Genes were functionally annotated using InterProScan version 5.19-58.0 (Jones *et al*,
198 2014). Protein families (PFAM) domain and gene ontology (GO) terms were assigned using hidden
199 Markov models (HMM). Secretion signals, transmembrane, cytoplasmic, and extracellular domains
200 were predicted using SignalP version 4.1 (Petersen *et al*, 2011), Phobius version 1.01 (Käll *et al*,
201 2004), and TMHMM version 2.0 (Krogh *et al*, 2001). A protein was conservatively considered as
202 secreted only if SignalP and Phobius both predicted a secretion signal and no transmembrane domain
203 was identified by either Phobius or TMHMM. Small secreted proteins were defined as secreted
204 proteins shorter than 300 amino acids. Detailed gene annotations are provided in Supplementary Table
205 S1. For plant cell wall degrading enzymes, i.e. enzymes involved in pectin, cellulose and
206 hemicellulose and lignin degradation we relied on the annotations and categorization of Sipos *et al*
207 (2017) (Supplementary Table S2). Similarly, we considered pathogenicity-related genes (including
208 secondary metabolite genes) as identified by Sipos *et al* (2017) (Supplementary Table S3).

209

210

211 **Results**

212

213 *Anchoring of the genome assembly to near chromosome-scale sequences*

214 The genome of *A. ostoyae* strain C18/9 was sequenced using PacBio and Illumina sequencing
215 technologies. PacBio reads were assembled into 106 scaffolds ranging from 5.0 kb to 6.4 Mb and
216 polished using Illumina reads (Sipos *et al*, 2017). The total assembled genome size was 60.1 Mb.
217 Here, we used a genetic map constructed for *A. ostoyae* strain C15 to assemble the genomic scaffolds
218 into putative chromosomes (or pseudochromosomes). The genetic map was based on 11,700 high-

219 quality SNP markers segregating in the mapping population. It contained 11 linkage groups and had a
220 total length of 1007.5 cM (Heinzelmann *et al*, 2017). We were able to anchor 61 of the 109 scaffolds,
221 which corresponds to 93% of the total sequence length of the genome assembly. The remaining 45
222 scaffolds were relatively short (5.0 to 338.3 kb). Overall, we observed a very high co-linearity of the
223 marker order in the genetic map and the reference genome. Discrepancies were found in 13 scaffolds
224 (scaffolds 1, 2, 4, 7, 9, 10, 12, 14, 16, 18, 27, 28 and 30). These scaffolds were split by the genetic map
225 into 2 - 4 fragments that individually mapped either to different linkage groups or to well separated
226 locations (i.e. > 650 kb apart) within the same linkage group (Supplementary Table S4). All scaffolds
227 splits were supported by multiple markers from different restriction sites. In addition, we found that a
228 part of scaffold 26 might be inverted or translocated in the genetic map relative to the reference
229 genome.

230

231 Based on the genetic map, most of the anchored scaffolds (87.2%) could be oriented within
232 pseudochromosomes (Table 1). Scaffolds (and fragments thereof) which could not be oriented ($n = 10$)
233 were all short (44.1 to 246.7 kb). Each of the constructed pseudochromosomes was composed of 4 to
234 10 scaffolds or scaffold fragments. The total length of pseudochromosomes ranged from 3.3 to 7.0
235 Mb. The assembly into pseudochromosomes anchored 19 scaffolds with terminal telomeric repeats
236 (TTAGGG)_{≥7}, which were all located at the extremities of pseudochromosomes. An additional
237 scaffold with terminal telomeric repeats could not be anchored. Overall, seven of the 11
238 pseudochromosomes had telomeres on both ends and the other four at one end, indicating that the
239 pseudochromosomes represent in most cases nearly complete chromosomes (Table 1). The shortest
240 pseudochromosome (LG 11) is substantially shorter than the others and might be missing a substantial
241 portion of a chromosomal arm.

242

243 *Frequency and distribution of crossover events*

244 In total, we identified 1984 crossover events among all 198 progeny and 11 pseudochromosomes.
245 The precision of crossover localization as determined by the spacing of SNP markers was below 20 kb
246 for 33.6% and below 50 kb for 68.6% of crossover events (Figure 1). Consecutive crossover events on
247 a chromosome were usually spaced far apart (Figure 1 and Supplementary Figure S1). On average, the

248 distance between consecutive crossover events was at least 3.7 Mb with the closest two events being
249 0.17 Mb and the most distant 6.8 Mb apart. The large distance between crossover events indicates that
250 most represent true crossovers, as non-crossovers are expected at much shorter distances. The possibly
251 incomplete pseudochromosome LG 11 was discarded from the above analysis. The total number of
252 crossover events observed per pseudochromosome varied from 115 (LG 11) to 214 (LG 1) (Table 2).
253 The number of crossover events per progeny and chromosome varied from 0 to 3 with a median count
254 of 1. Observing 3 crossovers on a chromosome was rare. We found no progeny with 3 crossovers on
255 LG 2, LG 10 and LG 11 and a maximum of 7 progeny with 3 crossovers on LG 3. Pseudochromosome
256 LG 11 had a very low mean crossover count compared to the other pseudochromosomes (0.58 vs. 0.80
257 - 1.08). On LG 11, only 4.5% of progeny were showing ≥ 2 crossover events compared to the other
258 pseudochromosomes where 16 - 30% of progeny were showing 2 or 3 crossover events. This suggests
259 that LG 11 is possibly missing a major part of a chromosomal arm without evidence what sequence
260 constitutes the missing chromosomal fragment.

261

262 *Heterogeneity of recombination rate along pseudochromosomes*

263 The recombination rates estimated in non-overlapping 20 kb segments along pseudochromosomes
264 were highly heterogeneous and varied from 0 to 737 cM/Mb (Figure 2). The median recombination
265 rate was 2.5 cM/Mb. We tested whether the degree of heterogeneity along pseudochromosomes was
266 deviating from a random distribution. When all pseudochromosomes (except pseudochromosome LG
267 11) were tested together, the recombination rate distribution was significantly different than a random
268 distribution (Fisher's exact test, $P < 10^{-6}$, lambda of simulated distribution = 0.29). When tested
269 individually, the recombination rate heterogeneity was significantly different than random on all but
270 three pseudochromosomes (Table 3). In general, the highest recombination rates were observed
271 towards the telomeres (Figure 2). We observed an inverse relationship of pseudochromosome length
272 and recombination rate ($r_{\text{Pearson}} = -0.77$, $P = 0.009$, pseudochromosome LG 11 excluded).

273

274 *Recombination hotspots*

275 We defined recombination hotspots as narrow chromosomal tracts with the highest recombination
276 rates. For this, we selected tracts of 20 kb chromosomal segments with recombination rates ≥ 200

277 cM/Mb. Both, the average and median recombination rate per 20 kb segment were with values of 17.6
278 cM/Mb and 2.5 cM/Mb, respectively, substantially lower. The probability to observe a 20 kb segment
279 with a recombination rate of ≥ 200 cM/Mb by chance was $P = 4.8 \times 10^{-4}$ (Poisson distribution with
280 $\lambda = 0.35$ cM, which equals the average genetic distance per segment). In total, we identified 30
281 segments of 20 kb with recombination rates ≥ 200 cM/Mb. These segments represent only 1.1% of the
282 analyzed genome sequence, but they accounted for 20.6% of the cumulative recombination rate.
283 Overall, we found 19 distinct recombination hotspots on LG 1 to LG 10 (Figure 2). While
284 pseudochromosome LG 11 was excluded from the above analyses, including LG 11 did not
285 meaningfully affect the outcome of the above analyses (data not shown). On LG 11, we also identified
286 two recombination hotspots (Figure 2).

287

288 *Association of recombination hotspots with sequence characteristics and gene content*

289 *A. ostoyae* has a gene dense genome composed of 45.6% coding sequences (both when analyzing
290 the complete scaffold assembly and the pseudochromosomes). The pseudochromosomes contained
291 slightly less genes (21350 vs. 22705) compared to the complete scaffold assembly. The reduction in
292 BUSCO completeness was reduced from 95.6% in the complete scaffold assembly to 95.2% in the
293 pseudochromosomes. The content of transposable elements in the *A. ostoyae* genome is moderate
294 (18.7% in the complete scaffold assembly and 14.5% in pseudochromosomes). Transposable elements
295 tend to cluster and coincide with chromosomal regions with a lower GC-content and lower coding
296 sequence density (Figure 3).

297

298 We found that recombination hotspots (defined as 50 kb windows centered on identified hotspots)
299 had a significantly lower density in coding sequences compared to the genomic background ($32.4 \pm$
300 10.5% (\pm standard deviation) vs. $45.7 \pm 13.4\%$; Mann–Whitney U test, $W = 4482$, $P = 2.9 \times 10^{-5}$)
301 (Figure 4). The density of transposable elements in recombination hotspots was not significantly
302 different to the genomic background ($8.0 \pm 8.1\%$ vs. $14.2 \pm 18.6\%$; Mann–Whitney U test, $W = 9826$,
303 $P = 0.798$) (Figure 4). Transposable element densities varied widely among windows. The median
304 hotspot window had a transposable element density of 4.8% compared to the 5.4% in the genomic

305 background. GC-content was nearly identical in recombination hotspots and the genomic background
306 ($48.3 \pm 0.8\%$ vs. $48.4 \pm 1.2\%$; Mann–Whitney U test, $W = 8337$, $P = 0.145$) (Figure 4).

307

308 We found that genes overlapping with recombination hotspots were encoding on average shorter
309 proteins (Mann–Whitney U test, $W = 2752400$, $P = 9.6 \times 10^{-8}$) (Figure 4). Protein length averaged
310 322.8 ± 268.1 amino acids in recombination hotspots and 406.1 ± 339.4 amino acids in the genomic
311 background. Proteins encoded in recombination hotspots were less likely to contain conserved PFAM
312 domains (Fisher’s exact test, $P = 8.2 \times 10^{-5}$) compared to the genomic background (34.9% vs. 45.7%)
313 (Figure 4). In the chromosomal context, we noted a lower density of genes with conserved PFAM
314 domains at chromosome peripheries compared to chromosome centers (Figure 5). The frequency of
315 genes encoding secreted proteins as well as small secreted proteins (< 300 aa) we found to be similar
316 between recombination hotspots and the genomic background (Supplementary Table S5). Next, we
317 analyzed plant cell wall degrading enzymes. Genes encoding pectin degrading enzymes were
318 significantly overrepresented in recombination hotspots compared to the genomic background
319 (Fisher’s exact test, $P = 0.007$) whereas genes encoding cellulose, hemicellulose and lignin degrading
320 enzymes were similarly distributed among hotspots and the genomic background (Figure 4 and
321 Supplementary Table S5). Pathogenicity-related genes (Sipos *et al*, 2017) tended to be more frequent
322 in hotspots vs. non-hotspot regions, but the difference was not statistically significant (Supplementary
323 Table S5). Overall, pathogenicity-related genes showed mostly a scattered distribution among all
324 pseudochromosomes except for LG 6 where a large cluster of pathogenicity-related genes was
325 observed (Figure 5). While pseudochromosome LG 11 was excluded from the above analyses,
326 including LG 11 did not meaningfully affect the outcome of the above analyses (data not shown).

327

328

329 Discussion

330

331 We constructed a dense genetic map for *A. ostoyae* that enabled assembling a chromosome-scale
332 reference genome. The presence of telomeric repeats on all but four pseudochromosomal ends

333 indicates that nearly all chromosomes are completely assembled. Recombination rates increased from
334 central regions towards the pseudochromosomal ends (*i.e.* telomeres). This further confirms the
335 reliability of the chromosomal assembly. In addition, all chromosomes contain a putative centromere
336 region of variable length (Figure 3), which is, as in other fungi, characterized by high transposable
337 element density, low gene density, absence of gene transcription and reduced CG-content (Müller *et*
338 *al.*, 2019; Smith *et al.*, 2012; Yadav *et al.*, 2018). Putative centromere regions were located within
339 chromosomal regions avoid of recombination, consistent with the findings from other fungi (Laurent
340 *et al.*, 2018; Mancera *et al.*, 2008; Müller *et al.*, 2019). The exact location and length of centromere
341 regions, however, needs to be confirmed using chromatin immunoprecipitation sequencing (CHIPseq)
342 as applied in other basidiomycetes (Yadav *et al.*, 2018).

343

344 The previous assembly of the *A. ostoyae* genome into sub-chromosomal scaffolds was highly
345 complete as assessed by BUSCO (Sipos *et al.*, 2017). Even though we were unable to place ~ 7% of
346 the total scaffold sequences, the unplaced scaffolds seem to contain mostly repetitive sequences. This
347 was evident from the fact that our chromosome-scale assembly had only a very slightly reduced
348 assembly completeness (95.2% *vs.* 95.6% of BUSCO genes). The transposable element content of our
349 assembly is indeed quite lower compared to the scaffold-level assembly (14.5% *vs.* 18.7%). The status
350 of the unplaced, repeat-rich scaffolds is difficult to assess. Our genetic map clearly lacked sufficient
351 reliable markers to place small, repeat-rich scaffolds. We also identified a small number of
352 discrepancies between the assembled scaffolds and the corresponding genetic map. These
353 discrepancies were in all cases disjunctions of scaffolds and may be due to genetic differences between
354 the sequenced strain (SBI C18/9) and the parental strain used for genetic mapping (C15). Some
355 discrepancies may also stem from scaffold assembly errors. To fully resolve the causes for these
356 discrepancies additional long-read sequencing is necessary. The pseudochromosome LG 11 is less
357 complete and likely misses a substantial part of a chromosomal arm. This was evident from the short
358 genetic map length and the markedly reduced number of progeny with at least 2 crossover events
359 compared to the other pseudochromosomes (4.5% *vs.* 16 - 30%). The missing sequence may contain
360 the rDNA cluster, which is challenging to assemble even with long-read sequencing and may

361 constitute a substantial fraction of a fungal chromosome (Sonnenberg *et al*, 2016; Van Kan *et al*,
362 2017). The scaffold assembly of *A. ostoyae* contains a scaffold with three units of the rDNA repeat.
363 However, we were unable to place this scaffold supporting the idea that our LG 11 assembly lacks the
364 rDNA repeat. Alternatively, the missing chromosomal fragment may represent a major structural
365 variation segregating between the strains SBI C18/9 and C15.

366

367 The identification of 11 pseudochromosomes (or linkage groups) provides the first estimate of the
368 haploid chromosome number for an *Armillaria* species. Other species from the order Agaricales were
369 found to have similar chromosome numbers: e.g. *Agaricus bisporus* ($n = 13$, Sonnenberg *et al*, 1996),
370 *Coprinopsis cinerea* ($n = 13$, Muraguchi *et al*, 2003), *Pleurotus ostreatus* ($n = 11$, Larraya *et al*, 1999)
371 or *Laccaria montana* ($n = 9$, Mueller *et al*, 1993). Given that our genetic map reached marker
372 saturation and covers 93% of the scaffold-level assembly, the presence of additional chromosomes is
373 highly unlikely. Karyotyping (*e.g.* by pulsed field gel electrophoresis) and high-density optical
374 mapping would provide further confirmation of chromosome numbers and sizes, and likely resolve the
375 placement of the remaining scaffolds. In particular, an optical map may help to resolve the size and
376 position of the highly repetitive rDNA cluster (Van Kan *et al*, 2017).

377

378 The total size of the genetic map for *A. ostoyae* was 1007.5 cM and falls into the range of genetic
379 map sizes observed for other basidiomycetes (Foulongne-Oriol, 2012). However, the total genetic map
380 size depends on chromosome numbers and chromosomal recombination rates, which both vary
381 substantially among fungal species. The *A. ostoyae* chromosomes all had a map length of 80.6-108.6
382 cM (with the exception of LG 11). This represents approximately two crossover events per bivalent
383 and meiosis, which is consistent with the number of progeny observed with 0 (~25%), or 1 (~50%) or
384 2 (~25%) crossovers per chromosome. Chromosomal crossover counts vary considerably among
385 fungal species. For example, in *A. bisporus* there is on average just one obligate crossover per bivalent
386 for all chromosomes (Sonnenberg *et al*, 2016), whereas in *Saccharomyces cerevisiae* the average is ~6
387 crossovers per bivalent (Mancera *et al*, 2008). Interestingly, in some fungi there is a strong positive

388 correlation between chromosomes size and the number of crossovers (Mancera *et al*, 2008; Roth *et al*,
389 2018), but we found no such apparent correlation in *A. ostoyae*.

390

391 The recombination landscape of *A. ostoyae* follows a canonical pattern, with increased
392 recombination towards the peripheries of chromosomes and decreased recombination towards
393 centromeres. The most striking deviations in these patterns are recombination hotspots. Such
394 recombination hotspots are observed in many fungal species (Croll *et al*, 2015; Laurent *et al*, 2018;
395 Müller *et al*, 2019; Roth *et al*, 2018; Van Kan *et al*, 2017), however their specific role in genome and
396 gene evolution is still largely unknown. In the wheat pathogen *Zymoseptoria tritici* recombination
397 hotspots may serve as ephemeral genome compartments favoring the emergence of fast-evolving
398 virulence genes (Croll *et al*, 2015). Recombination hotspots in *A. ostoyae* were with two exceptions all
399 located at the peripheries of chromosomes, where gene densities are low and gene functions are less
400 conserved. From an evolutionary perspective, placing recombination hotspots distal from conserved
401 housekeeping genes should be favorable given the mutagenic potential of hotspots. Interestingly, we
402 found that genes involved in pectin degradation were enriched in recombination hotspots compared to
403 the genomic background. Pectin is a major component of the plant cell wall and pectinolytic enzymes
404 are among the first enzymes secreted by plant pathogens during host infection (Herbert *et al*, 2003).
405 However, pectinolytic enzymes may also serve as effectors and induce plant defense reactions
406 (Herbert *et al*, 2003). Hence, rapid evolution of pectinolytic enzymes may provide an advantage to
407 *Armillaria* in its arms race with its hosts.

408

409

410 **Acknowledgments**

411

412 Sequencing libraries were generated in collaboration with the Genetic Diversity Center (GDC) of
413 ETH Zurich and sequenced by the Quantitative Genomics Facility of the Department of Biosystems
414 Science and Engineering (D-BSSE) of ETH Zurich in Basel. The *A. ostoyae* genome project was

415 funded by the European Union in the framework of the Széchenyi 2020 Program (GINOP-2.3.2-15-
416 2016-00052) to GS and MM and by the WSL to GS.

417

418

419 **Conflict of interest**

420

421 The authors declare that they have no conflict of interest.

422

423 **Data availability**

424

425 Progeny sequencing data is available on the NCBI SRA under the BioProject accession
426 PRJNA380873. The updated genome assembly was submitted to the European Nucleotide Archive
427 (new accession number pending). The previous scaffold assembly can be retrieved from European
428 Nucleotide Archive under the accession FUEG01000000.

429

430

431 **Supplementary information**

432

433 Supplementary Figures and Tables are available.

434

435 **References**

436

437 Anderson JB, Ullrich RC (1979). Biological species of *Armillaria mellea* in North America.

438 *Mycologia* **71**: 402-414.

439 Aylward J, Steenkamp ET, Dreyer LL, Roets F, Wingfield BD, Wingfield MJ (2017). A plant

440 pathology perspective of fungal genome sequencing. *IMA Fungus* **8**: 1-15.

441 Bendel M, Kienast F, Rigling D, Bugmann H (2006). Impact of root-rot pathogens on forest

442 succession in unmanaged *Pinus mugo* stands in the Central Alps. *Can J For Res* **36**: 2666-2674.

443 Broman KW, Wu H, Sen S, Churchill GA (2003). R/qtl: QTL mapping in experimental crosses.

444 *Bioinformatics* **19**: 889-890.

445 Charlesworth B, Harvey PH, Charlesworth B, Charlesworth D (2000). The degeneration of Y

446 chromosomes. *Philos Trans Royal Soc B* **355**: 1563-1572.

447 Collins C, Keane TM, Turner DJ, O’Keeffe G, Fitzpatrick DA, Doyle S (2013). Genomic and

448 proteomic dissection of the ubiquitous plant pathogen, *Armillaria mellea*: toward a new infection

449 model system. *J Proteome Res* **12**: 2552-2570.

450 Croll D, Lendenmann MH, Stewart E, McDonald BA (2015). The impact of recombination hotspots

451 on genome evolution of a fungal plant pathogen. *Genetics* **201**: 1213-1228.

452 Didelot X, Achtman M, Parkhill J, Thomson NR, Falush D (2007). A bimodal pattern of relatedness

453 between the *Salmonella* Paratyphi A and Typhi genomes: convergence or divergence by

454 homologous recombination? *Genome Res* **17**: 61-68.

455 Fledel-Alon A, Wilson DJ, Broman K, Wen X, Ober C, Coop G *et al* (2009). Broad-scale

456 recombination patterns underlying proper disjunction in humans. *PLOS Genet* **5**: e1000658.

457 Foulongne-Oriol M (2012). Genetic linkage mapping in fungi: current state, applications, and future

458 trends. *Appl Microbiol Biotechnol* **95**: 891-904.

459 Guillaumin JJ, Legrand P, Lung-Escarmant B, Botton B (eds) (2005). *L’armillaire et le pourridié-*

460 *agaric des végétaux ligneux*. INRA: Paris, pp 487.

- 461 Guillaumin JJ, Mohammed C, Anselmi N, Courtecuisse R, Gregory SC, Holdenrieder O *et al* (1993).
462 Geographical distribution and ecology of the *Armillaria* species in western Europe. *Eur J Forest*
463 *Pathol* **23**: 321-341.
- 464 Haenel Q, Laurentino TG, Roesti M, Berner D (2018). Meta-analysis of chromosome-scale crossover
465 rate variation in eukaryotes and its significance to evolutionary genomics. *Mol Ecol* **27**: 2477-
466 2497.
- 467 Hamilton WD (1980). Sex versus non-sex versus parasite. *Oikos* **35**: 282-290.
- 468 Hassold T, Hunt P (2001). To err (meiotically) is human: the genesis of human aneuploidy. *Nat Rev*
469 *Genet* **2**: 280-291.
- 470 Heinzelmann R, Croll D, Zoller S, Sipos G, Münsterkötter M, Güldener U *et al* (2017). High-density
471 genetic mapping identifies the genetic basis of a natural colony morphology mutant in the root rot
472 pathogen *Armillaria ostoyae*. *Fungal Genet Biol* **108**: 44-54.
- 473 Heinzelmann R, Dutech C, Tsykun T, Labbé F, Soularue J-P, Prospero S (2019). Latest advances and
474 future perspectives in *Armillaria* research. *Can J Plant Pathol* **41**: 1-23.
- 475 Herbert C, Boudart G, Borel C, Jacquet C, Esquerre-Tugaye M, Dumas B (2003). Regulation and role
476 of pectinases in phytopathogenic fungi. In: Voragen F, Schols H and Visser R (eds) *Advances in*
477 *pectin and pectinase research*. Springer: Dordrecht, pp 201-220.
- 478 Hill WG, Robertson A (2009). The effect of linkage on limits to artificial selection. *Genet Res* **8**: 269-
479 294.
- 480 Holt KE, Parkhill J, Mazzoni CJ, Roumagnac P, Weill F-X, Goodhead I *et al* (2008). High-throughput
481 sequencing provides insights into genome variation and evolution in *Salmonella typhi*. *Nat Genet*
482 **40**: 987.
- 483 Hood IA, Redfern DB, Kile GA (1991). *Armillaria* in planted hosts. In: Shaw III CG and Kile GA
484 (eds) *Armillaria root disease. Agricultural Handbook No. 691*. USDA Forest Service:
485 Washington D.C., pp 122-149.
- 486 Jones P, Binns D, Chang H-Y, Fraser M, Li W, McAnulla C *et al* (2014). InterProScan 5: genome-
487 scale protein function classification. *Bioinformatics* **30**: 1236-1240.

- 488 Käll L, Krogh A, Sonnhammer ELL (2004). A combined transmembrane topology and signal peptide
489 prediction method. *J Mol Biol* **338**: 1027-1036.
- 490 Krogh A, Larsson B, von Heijne G, Sonnhammer ELL (2001). Predicting transmembrane protein
491 topology with a hidden markov model: application to complete genomes. *J Mol Biol* **305**: 567-
492 580.
- 493 Laflamme G, Guillaumin JJ (2005). L'armillaire, agent pathogène mondial: répartition et dégâts. In:
494 Guillaumin JJ, Legrand P, Lung-Escarmant B and Botton B (eds) *L' armillaire et la pourridié-*
495 *agaric des végétaux ligneux*. INRA: Paris, pp 273-289.
- 496 Larraya LM, Perez G, Penas MM, Baars JJP, Mikosch TSP, Pisabarro AG *et al* (1999). Molecular
497 karyotype of the white rot fungus *Pleurotus ostreatus*. *Appl Environ Microbiol* **65**: 3413-3417.
- 498 Laurent B, Palaiokostas C, Spataro C, Moinard M, Zehraoui E, Houston RD *et al* (2018). High-
499 resolution mapping of the recombination landscape of the phytopathogen *Fusarium graminearum*
500 suggests two-speed genome evolution. *Mol Plant Pathol* **19**: 341-354.
- 501 Lively CM (2010). A review of red queen models for the persistence of obligate sexual reproduction. *J*
502 *Hered* **101**: S13-S20.
- 503 Mancera E, Bourgon R, Brozzi A, Huber W, Steinmetz LM (2008). High-resolution mapping of
504 meiotic crossovers and non-crossovers in yeast. *Nature* **454**: 479-485.
- 505 McDonald BA, Linde C (2002). Pathogen population genetics, evolutionary potential, and durable
506 resistance. *Annu Rev Phytopathol* **40**: 349-379.
- 507 McLaughlin JA (2001). Impact of Armillaria root disease on succession in red pine plantations in
508 southern Ontario. *For Chron* **77**: 519-524.
- 509 Möller M, Stukenbrock EH (2017). Evolution and genome architecture in fungal plant pathogens. *Nat*
510 *Rev Micro* **15**: 756.
- 511 Morran LT, Schmidt OG, Gelarden IA, Parrish RC, Lively CM (2011). Running with the red queen:
512 Host-parasite coevolution selects for biparental sex. *Science* **333**: 216-218.
- 513 Morrison DJ, Chu D, Johnson ALS (1985). Species of *Armillaria* in British-Columbia. *Can J Plant*
514 *Pathol* **7**: 242-246.

- 515 Mueller GJ, Mueller GM, Shih L-H, Ammirati JF (1993). Cytological Studies in *Laccaria*
516 (Agaricales). I. Meiosis and postmeiotic mitosis. *Am J Bot* **80**: 316-321.
- 517 Müller MC, Praz CR, Sotiropoulos AG, Menardo F, Kunz L, Schudel S *et al* (2019). A chromosome-
518 scale genome assembly reveals a highly dynamic effector repertoire of wheat powdery mildew.
519 *New Phytol* **221**: 2176-2189.
- 520 Muraguchi H, Ito Y, Kamada T, Yanagi SO (2003). A linkage map of the basidiomycete *Coprinus*
521 *cinereus* based on random amplified polymorphic DNAs and restriction fragment length
522 polymorphisms. *Fungal Genet Biol* **40**: 93-102.
- 523 Nelson MI, Holmes EC (2007). The evolution of epidemic influenza. *Nat Rev Genet* **8**: 196.
- 524 Ota Y, Matsushita N, Nagasawa E, Terashita T, Fukuda K, Suzuki K (1998). Biological species of
525 *Armillaria* in Japan. *Plant Dis* **82**: 537-543.
- 526 Otto SP, Barton NH (1997). The evolution of recombination: removing the limits to natural selection.
527 *Genetics* **147**: 879-906.
- 528 Otto SP, Lenormand T (2002). Resolving the paradox of sex and recombination. *Nat Rev Genet* **3**:
529 252-261.
- 530 Petersen TN, Brunak S, von Heijne G, Nielsen H (2011). SignalP 4.0: discriminating signal peptides
531 from transmembrane regions. *Nat Methods* **8**: 785-786.
- 532 Prospero S, Holdenrieder O, Rigling D (2004). Comparison of the virulence of *Armillaria cepistipes*
533 and *Armillaria ostoyae* on four Norway spruce provenances. *Forest Pathol* **34**: 1-14.
- 534 Qin GF, Zhao J, Korhonen K (2007). A study on intersterility groups of *Armillaria* in China.
535 *Mycologia* **99**: 430-441.
- 536 R Development Core Team (2017). R: A language and environment for statistical computing. R
537 Foundation for Statistical Computing. Vienna, Austria.
- 538 Roth C, Sun S, Billmyre RB, Heitman J, Magwene PM (2018). A high-resolution map of meiotic
539 recombination in *Cryptococcus deneoformans* demonstrates decreased recombination in
540 unisexual reproduction. *Genetics* **209**: 567-578.

- 541 Sánchez-Vallet A, Fouché S, Fudal I, Hartmann FE, Soyer JL, Tellier A *et al* (2018). The genome
542 biology of effector gene evolution in filamentous plant pathogens. *Annu Rev Phytopathol* **56**: 21-
543 40.
- 544 Shaw III CG, Kile GA (eds) (1991). *Armillaria root disease. Agricultural Handbook No. 691*. USDA
545 Forest Service: Washington D.C., pp 233.
- 546 Simão FA, Waterhouse RM, Ioannidis P, Kriventseva EV, Zdobnov EM (2015). BUSCO: assessing
547 genome assembly and annotation completeness with single-copy orthologs. *Bioinformatics* **31**:
548 3210-3212.
- 549 Sipos G, Prasanna AN, Walter MC, O'Connor E, Bálint B, Krizsán K *et al* (2017). Genome expansion
550 and lineage-specific genetic innovations in the forest pathogenic fungi *Armillaria*. *Nat Ecol Evol*
551 **1**: 1931-1941.
- 552 Smith KM, Galazka JM, Phatale PA, Connolly LR, Freitag M (2012). Centromeres of filamentous
553 fungi. *Chromosome Res* **20**: 635-656.
- 554 Sonnenberg ASM, de Groot PW, Schaap PJ, Baars JJP, Visser J, Van Griensven LJ (1996). Isolation
555 of expressed sequence tags of *Agaricus bisporus* and their assignment to chromosomes. *Appl*
556 *Environ Microbiol* **62**: 4542-4547.
- 557 Sonnenberg ASM, Gao W, Lavrijssen B, Hendrickx P, Sedaghat-Tellgerd N, Foulongne-Oriol M *et al*
558 (2016). A detailed analysis of the recombination landscape of the button mushroom *Agaricus*
559 *bisporus* var. *bisporus*. *Fungal Genet Biol* **93**: 35-45.
- 560 Stukenbrock EH, Dutheil JY (2018). Fine-scale recombination maps of fungal plant pathogens reveal
561 dynamic recombination landscapes and intragenic hotspots. *Genetics* **208**: 1209-1229.
- 562 Stukenbrock EH, McDonald BA (2008). The origins of plant pathogens in agro-ecosystems. *Annu Rev*
563 *Phytopathol* **46**: 75-100.
- 564 Taylor J, Butler D (2017). R Package ASMap: Efficient Genetic Linkage Map Construction and
565 Diagnosis. *J Stat Softw* **79**: 1–29.
- 566 Van Kan JAL, Stassen JHM, Mosbach A, Van Der Lee TAJ, Faino L, Farmer AD *et al* (2017). A
567 gapless genome sequence of the fungus *Botrytis cinerea*. *Mol Plant Pathol* **18**: 75-89.

- 568 Wendte JM, Miller MA, Lambourn DM, Magargal SL, Jessup DA, Grigg ME (2010). Self-mating in
569 the definitive host potentiates clonal outbreaks of the apicomplexan parasites *Sarcocystis neurona*
570 and *Toxoplasma gondii*. *PLOS Genet* **6**: e1001261.
- 571 Wilson MA, Makova KD (2009). Genomic analyses of sex chromosome evolution. *Annu Rev Genom*
572 *Hum G* **10**: 333-354.
- 573 Wingfield BD, Ambler JM, Coetzee MPA, de Beer ZW, Duong TA, Joubert F *et al* (2016). Draft
574 genome sequences of *Armillaria fuscipes*, *Ceratocystiopsis minuta*, *Ceratocystis adiposa*,
575 *Endoconidiophora laricicola*, *E. polonica* and *Penicillium frei* DAOMC 242723. *IMA Fungus* **7**:
576 217-227.
- 577 Wu YH, Bhat PR, Close TJ, Lonardi S (2008). Efficient and accurate construction of genetic linkage
578 maps from the minimum spanning tree of a graph. *PLOS Genet* **4**: e1000212.
- 579 Yadav V, Sun S, Billmyre RB, Thimmappa BC, Shea T, Lintner R *et al* (2018). RNAi is a critical
580 determinant of centromere evolution in closely related fungi. *Proc Natl Acad Sci USA* **115**: 3108-
581 3113.
- 582
- 583
- 584

585 **Figure legends**

586

587 **Figure 1.** Resolution of the genetic map constructed for *Armillaria ostoyae* strain C15, distance of
588 crossover events and accuracy of crossover placement. **A)** Physical distance between consecutive
589 markers (marker pairs associated with the same restriction site excluded, see Materials and Methods)
590 on pseudochromosomes LG 1 to LG 11. **B)** Physical distance of consecutive crossover events. The
591 shortest distance recorded is 0.17 Mb. Because a major part of the left chromosome arm of
592 pseudochromosome LG 11 may be missing, this pseudochromosome was excluded from this analysis.
593 **C)** Physical distance of the two markers flanking a crossover. All pseudochromosomes were included.

594

595 **Figure 2.** Recombination landscape of *Armillaria ostoyae* strain C15. Recombination rates were
596 estimated in non-overlapping 20 kb segments. Vertical grey bars indicate the location of
597 recombination hotspots defined as 50 kb windows centered on one or two adjacent 20 kb segments
598 with recombination rates ≥ 200 cM/Mb. A potential recombination hotspot on LG 1 at 6 Mb was not
599 considered a recombination hotspot because of an overlap with an assembly gap.

600

601 **Figure 3.** Characteristics of the *Armillaria ostoyae* pseudochromosomes. For each
602 pseudochromosome, the first panel shows the genetic map position vs. the physical position of SNP
603 markers (black dots). Gene density is shown in red and the density of transposable elements (TEs) is
604 shown in blue. The position of recombination hotspots is indicated by grey vertical bars. Stars indicate
605 approximate location of putative centromere regions. The second panel shows the GC content in
606 green. The gray dashed line indicates the average GC content across all pseudochromosomes. Gene
607 density, TE density and GC content were all estimated in non-overlapping 50 kb windows. The third
608 panel shows gene expression levels in the cap of a fruiting body of the diploid *A. ostoyae* strain C18,
609 which is the parental strain of the sequenced monosporous strain. Average gene expression among
610 three biological replicates is shown. Expression data are retrieved from Sipos et al. (2017). RPKM =
611 Reads per kilobase of transcript per million mapped reads. The fourth panel shows the position of

612 BUSCO genes. Complete single copy BUSCO genes are shown in red and duplicated BUSCO genes
613 are shown in blue.

614

615 **Figure 4.** Characteristics of recombination hotspots in comparison to the genomic background. **A)** GC
616 content, **B)** coding sequence density, **C)** density of transposable elements (TEs), **D)** protein length, **E)**
617 percentage of genes with conserved domains (i.e. with PFAM annotation) and **F)** percentage of plant
618 cell wall degrading genes (including pectin, cellulose, hemicellulose and lignin degrading genes) and
619 pathogenicity-related genes. **A-C)** were estimated for the genomic background in non-overlapping 50
620 kb windows.

621

622 **Figure 5.** Distribution of genes encoding plant cell wall degrading (PCWD) enzymes (top bar),
623 pathogenicity-related proteins (second bar), secreted proteins (third bar) and genes with conserved
624 domains (i.e. PFAM annotation) (bottom bar) along the pseudochromosomes of *Armillaria ostoyae*.
625 The following categories of plant cell wall degrading enzyme are distinguished: pectin degrading
626 enzymes (blue), cellulose and hemicellulose degrading enzymes (red) and lignin degrading enzymes
627 (black). Of the pathogenicity-related proteins, the three most frequent categories are highlighted:
628 NRPS-like synthases (black), hydrophobins (dark brown) and carboxylesterases (medium brown). All
629 other types of pathogenicity-related proteins are colored in light brown. Short secreted proteins (< 300
630 aa) are indicated in green, whereas all other secreted proteins are indicated in black. The density of
631 genes with conserved domains is highest in dark areas and lowest in brighter areas. The locations of
632 recombination hotspots are indicated by vertical gray bars spanning the horizontal bars.

633

634

635

636 **Tables**

637

638 **Table 1.** Overview of the pseudochromosomes constructed for *Armillaria ostoyae* based on the
 639 genetic map constructed in the progeny of the diploid *A. ostoyae* strain C15 and the genome assembly
 640 for the haploid *A. ostoyae* strain SBI C18/9.

641

Pseudochromosome	Physical length (bp)	Genetic map length (cM) ^a	Recombination rate (cM/Mb)	Number of scaffolds ^b	Left telomere ^c	Right telomere ^c
LG 1	6,974,893	108.6	15.6	10 (8)	X	X
LG 2	4,262,795	102.9	24.1	7 (7)	X	X ^d
LG 3	6,235,469	102.4	16.4	6 (6)	X	X
LG 4	5,066,647	98.9	19.5	9 (8)	X	–
LG 5	6,229,232	97.0	15.6	5 (5)	X	X
LG 6	4,611,551	93.9	20.4	9 (7)	X	X
LG 7	4,688,545	93.5	19.9	8 (7)	–	X
LG 8	5,329,788	89.0	16.7	8 (7)	X	X
LG 9	5,393,285	82.5	15.3	5 (3)	X	–
LG 10	4,532,110	80.6	17.8	7 (6)	X	X ^e
LG 11 ^f	3,341,870	58.2	17.4	4 (4)	–	X
Total	56,666,185	1007.5		78 (68)		

642

643 ^a Length of corresponding linkage group

644 ^b Number of scaffolds or scaffold fragments contained in the pseudochromosome; in parentheses, the number of
 645 scaffolds or scaffold fragments which could be orientated.

646 ^c X telomere present, – telomere absent.

647 ^d Telomere interrupted by ~ 200bp other sequence.

648 ^e Two consecutive scaffolds with terminal telomeric repeats. At least 200'000 bp other sequence between
 649 stretches of telomeric repeats.

650 ^f Pseudochromosome possibly incomplete.

651

652

653 **Table 2.** Overview of crossover counts per linkage group in the progeny of the diploid *A. ostoyae*
 654 strain C15.

655

Pseudochromosome	Occurrence of progeny with ... crossovers				Median crossover count	Mean crossover count	Crossover count per Mb	No. of crossovers total
	0	1	2	3				
LG 1	47	91	57	3	1.00	1.08	0.15	214
LG 2	44	106	48	0	1.00	1.02	0.24	202
LG 3	52	98	41	7	1.00	1.02	0.16	201
LG 4	51	101	45	1	1.00	0.98	0.19	194
LG 5	56	92	44	6	1.00	1.00	0.16	198
LG 6	60	97	37	4	1.00	0.92	0.20	183
LG 7	57	101	39	1	1.00	0.92	0.20	182
LG 8	60	102	35	1	1.00	0.88	0.17	175
LG 9	70	96	30	2	1.00	0.82	0.15	162
LG 10	74	90	34	0	1.00	0.80	0.18	158
LG 11 ^a	92	97	9	0	1.00	0.58	0.17	115
Total								1984

656

657 ^a Pseudochromosome possibly incomplete.

658

659 **Table 3.** Recombination rate heterogeneity tests for individual pseudochromosomes. The observed
660 distribution of recombination was compared to a Poisson distribution using Fisher's exact test.
661

Pseudochromosome	<i>P</i> -value ^a		Lambda ^b
LG 1	< 10 ⁻³	***	0.25
LG 2	0.534	ns	0.42
LG 3	< 10 ⁻³	***	0.27
LG 4	0.006	**	0.28
LG 5	0.085	ns	0.29
LG 6	0.031	*	0.34
LG 7	0.033	*	0.30
LG 8	0.002	**	0.26
LG 9	0.028	*	0.27
LG 10	0.648	ns	0.27
LG 11 ³⁾	-	-	-

662

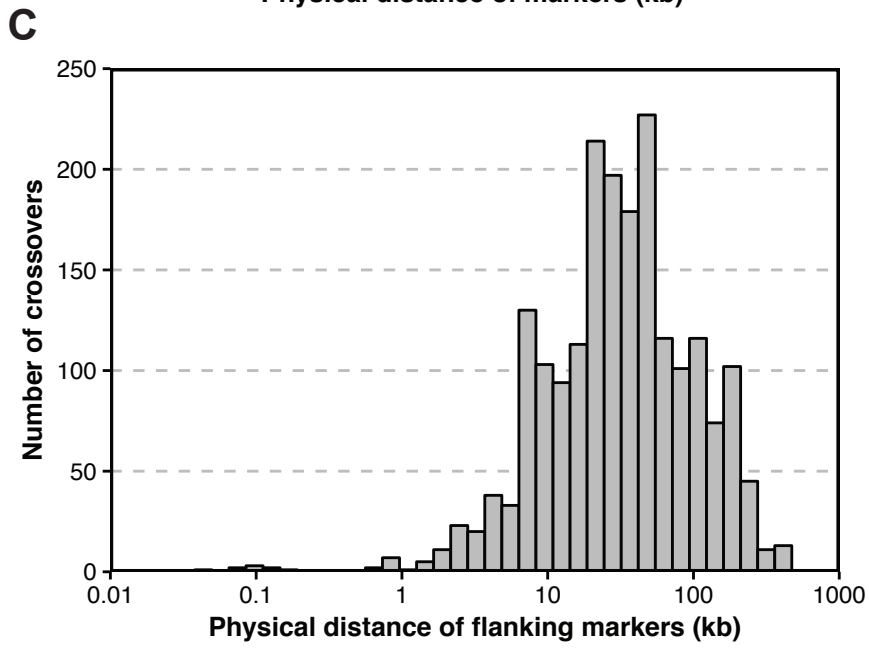
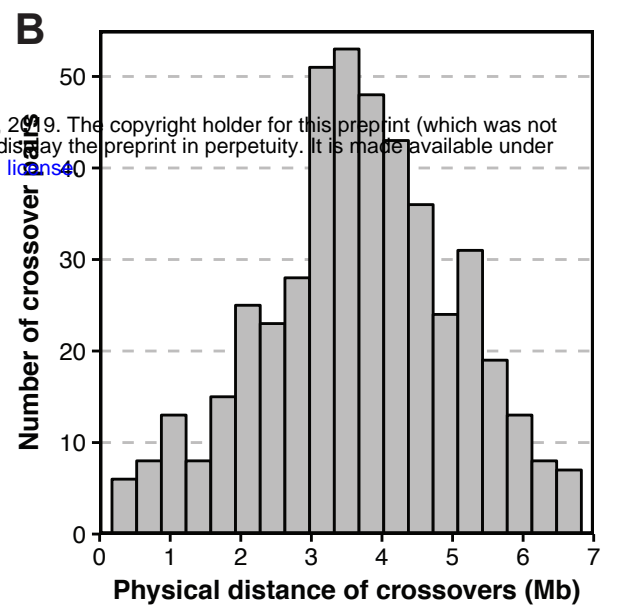
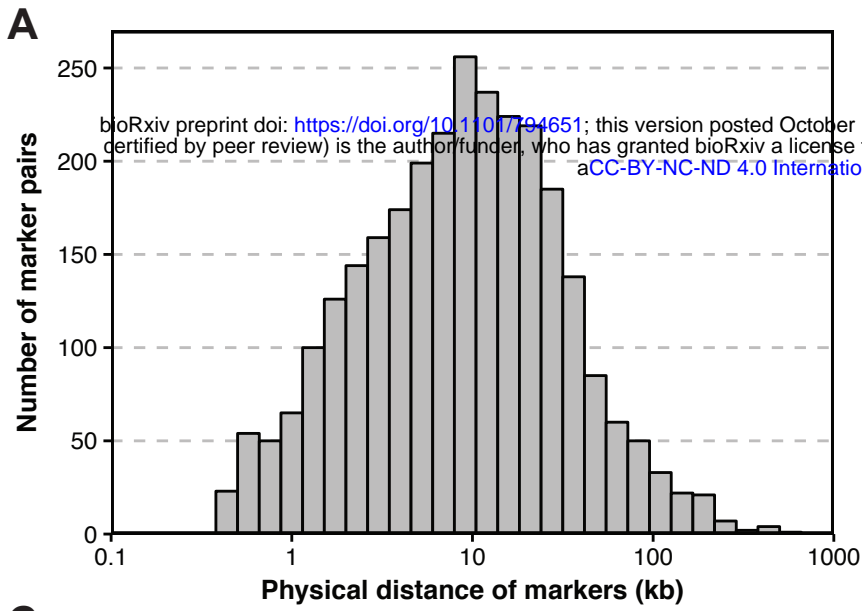
663 ^a * *P* < 0.05, ** *P* < 0.01, *** *P* < 0.001, ns: not significant.

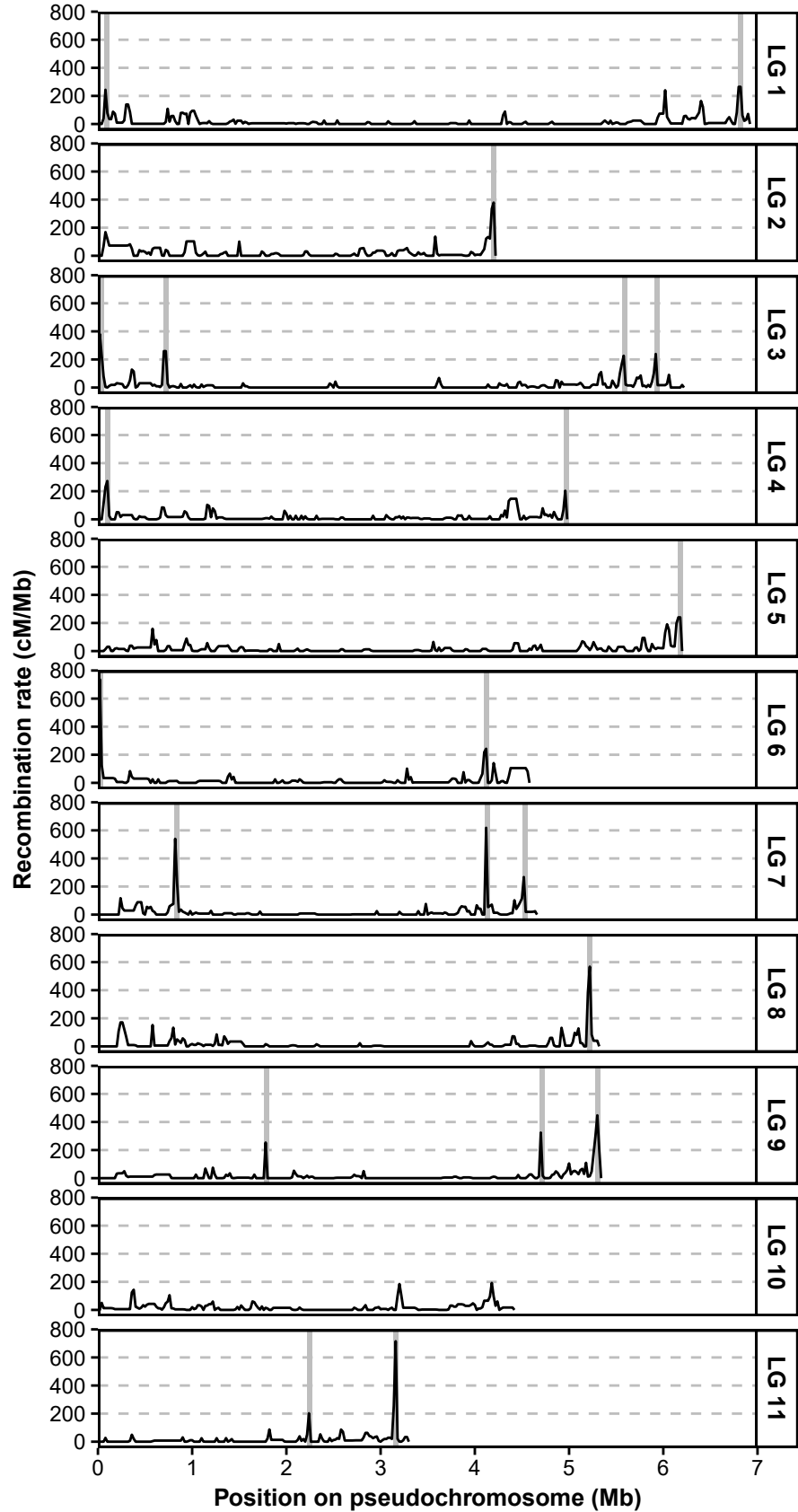
664 ^b Lambda used for simulation of reference Poisson distribution. For details see Materials and Methods.

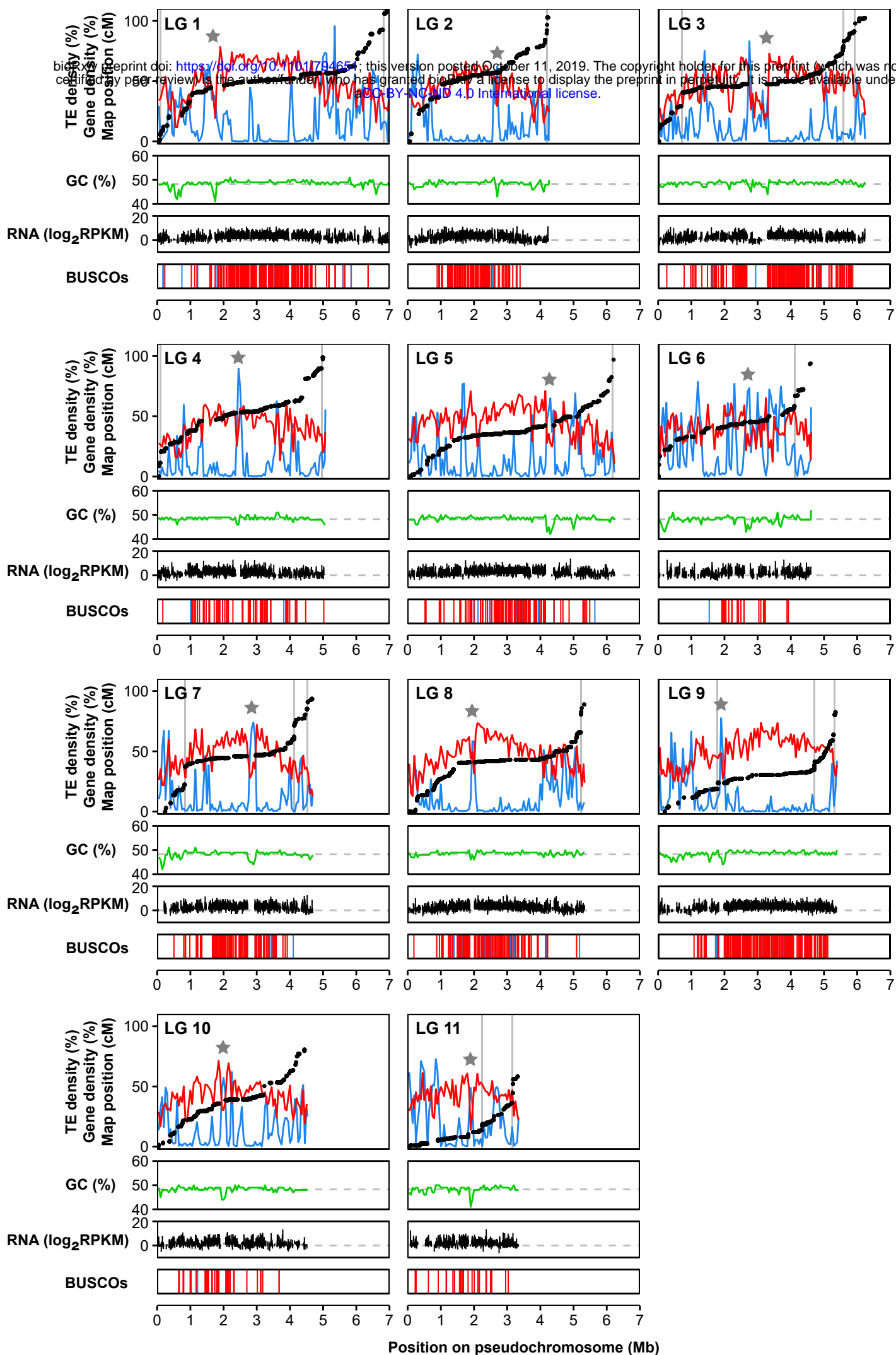
665 ^c No test was conducted as pseudochromosome is possibly incomplete.

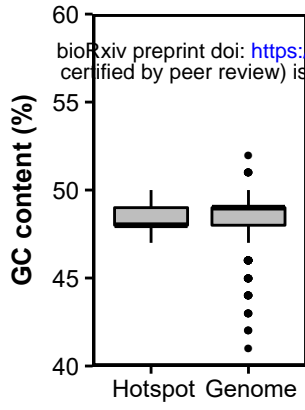
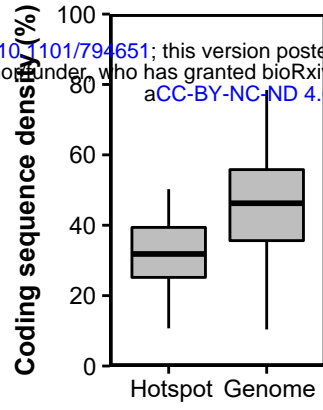
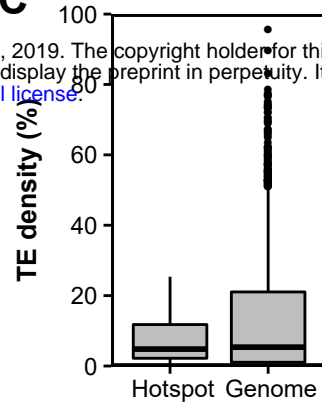
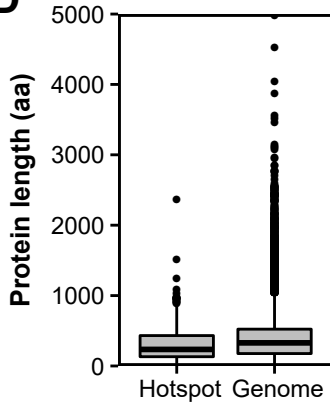
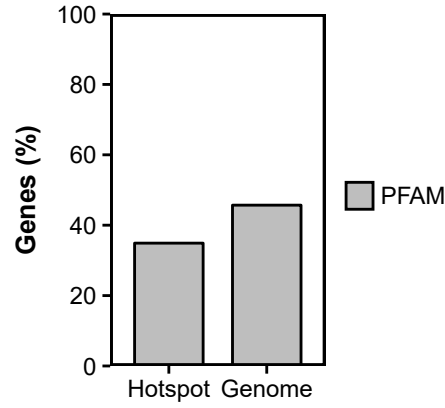
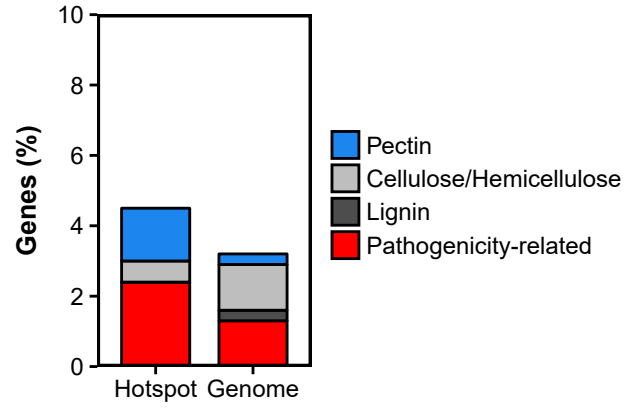
666

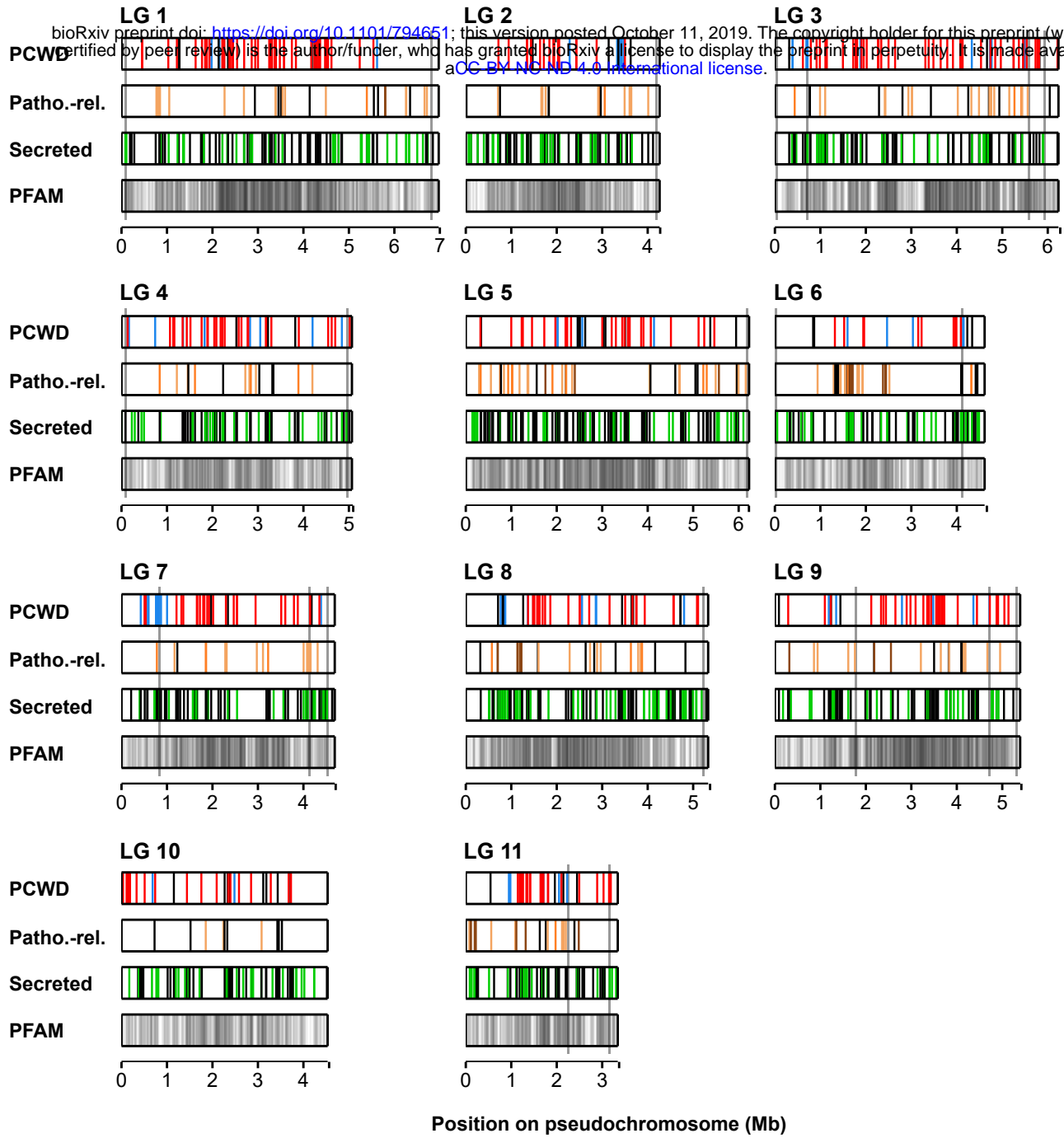
667







A**B****C****D****E****F**



Position on pseudochromosome (Mb)